

See discussions, stats, and author profiles for this publication at: <https://www.researchgate.net/publication/390771197>

# Study on the regulation of thermal decomposition of ammonium perchlorate by energetic composites formed with Fe-based coordination polymers

Article in *Advanced Powder Technology* · April 2025

DOI: 10.1016/j.apt.2025.104865

---

CITATIONS

0

READS

6

1 author:



Wei Zhou

Hunan University

17 PUBLICATIONS 747 CITATIONS

[SEE PROFILE](#)



ELSEVIER

Contents lists available at ScienceDirect

## Advanced Powder Technology

journal homepage: [www.elsevier.com/locate/apt](http://www.elsevier.com/locate/apt)

# Study on the regulation of thermal decomposition of ammonium perchlorate by energetic composites formed with Fe-based coordination polymers

Yan Zhao <sup>a,b,1</sup>, Xing Zhou <sup>a,1,\*</sup>, Hongfeng Ji <sup>c</sup>, Bian Li <sup>a</sup>, Wei Zhou <sup>a</sup>, Yao-Hua Liu <sup>a</sup>, Guixi Liu <sup>b</sup><sup>a</sup>College of Aerospace Science and Technology, National University of Defense Technology, Changsha 410073, PR China<sup>b</sup>Power Machinery Institute of Inner Mongolia, Hohhot 010010, PR China<sup>c</sup>Synthetic Chemical Engineering Institute of Inner Mongolia, Hohhot 010010, PR China

## ARTICLE INFO

## Article history:

Received 21 October 2024

Received in revised form 12 March 2025

Accepted 21 March 2025

## Keywords:

Coordination polymers

Ammonium perchlorate

Combustion catalyst

Controllable decomposition

## ABSTRACT

This study focuses on the thermal decomposition regulation behavior of AP achieved by Fe5B/AP nanoparticles, which are characterized using XRD, XPS and other techniques. When the mass ratio of Fe5B catalyst to AP was 3:1, the high-temperature peak associated with AP decomposition advanced significantly by 181 °C, resulting in a more concentrated exothermic process. Additionally, solid propellant containing an optimal mass ratio of 1:3 for Fe5B to AP exhibited higher burning velocity compared to Fe<sub>2</sub>O<sub>3</sub> under low pressure condition with a 10 % increase in burning rate. Within the pressure range from 3.0 MPa to 9.0 MPa, the combustion rate of solid propellant containing Fe5B/AP (1:3) remained similar to that achieved with Fe<sub>2</sub>O<sub>3</sub> but displayed a lower pressure index. The mechanistic studies show Fe-based structural units and active metal centers served as intermediates for electron transfer, expediting electron transfer between ClO<sub>4</sub><sup>-</sup> and NH<sub>4</sub><sup>+</sup> in the LTD process. Fe5B/AP particles generate iron oxides in situ, facilitating the adsorption of oxygen species and promoting increased heat release during the HTD stage. These findings highlight the potential application of Fe5B/AP as combustion catalysts for solid propellants by enabling controlled decomposition behavior of ammonium perchlorate.

© 2025 Published by Elsevier B.V. on behalf of The Society of Powder Technology Japan.

## 1. Introduction

Combustion catalysts are an effective means of regulating the combustion performance of solid propellants. Currently, widely studied combustion catalysts include metals and metal oxides [1,2], inorganic metal salts [3,4], metal-organic compounds [5,6], carbon nanomaterial-based combustion catalysts [7,8], and various energetic combustion catalysts [9–11]. By adding traditional burning rate catalysts, the thermal decomposition rate of the oxidizer can be increased. The production cost and technical threshold of classical combustion catalysts are relatively low, but their effect on improving combustion speed is limited. On the other hand, particle size is also a significant factor in the burning velocity of solid propellants [12]. With the development of new material technology and the application of new materials with nanostructures,

the composite energetic combustion catalysts effectively compensate for the low energy level of traditional metal oxide combustion catalysts and provide broader space for developing high-energy solid propellants [4,13]. It is of great significance to study composite burning rate catalysts with high energy passivity for solid propellants.

Coordination polymers (CPs) are a class of crystalline materials with diverse topologies and regular pores of specific sizes, formed by discrete metal ions or ion clusters and two- or multi-dentate ligands [14]. Transition metal ions, such as Cu, Fe, and Zn, are selectively employed to augment catalytic activity and function as the primary active sites for catalytic reactions. High-energy organic ligands with a substantial nitrogen content (molecules possessing extensive π bonds akin to benzene rings, excellent thermal stability, and low sensitivity) are employed [15]. The flexibility of metal ions and ligands, as well as their coordination modes, allows for effective regulation of the performance of energetic CPs [16–18]. Moreover, CPs exhibit a substantial specific surface area, regular pore structure [19,20], and highly dispersed metal active sites that facilitate the adsorption of perchloric acid and ammonia gases

\* Corresponding author.

E-mail address: [xingzhou\\_nudt@nudt.edu.cn](mailto:xingzhou_nudt@nudt.edu.cn) (X. Zhou).<sup>1</sup> These authors contributed to the work equally and should be regarded as co-first authors.

during the thermal decomposition process of ammonium perchlorate (AP). These characteristics make CPs potential high-efficiency solid propellant combustion catalysts. More recently, Yang et al. [21] investigated the effect of Fe-benzene-1,3,5-tricarboxylate (Fe-BTC) CPs on the thermal decomposition of ammonium perchlorate (AP) and the combustion performance of propellants with AP as an oxidant. They discovered that Fe-BTC itself can expedite the pyrolysis of AP. Furthermore, the  $\text{Fe}_2\text{O}_3@\text{C}$  generated in situ by Fe-BTCs decomposition is also an efficient combustion catalyst, indicating that introducing CPs into propellants can be served both as a combustion catalyst and a precursor to combustion catalysts. It has been verified that the catalytic activity exhibited by in-situ formed metal oxides through CPs' decomposition is higher than traditional ones [22,23].

Ammonium perchlorate is the most commonly utilized oxidant for composite solid propellants [24], and its combustion behavior can be influenced by its thermal decomposition characteristics [25]. Currently, a common approach to developing solid propellants suitable for solid rocket engines involves adjusting the decomposition characteristics through the addition of various types of combustion catalysts [26,27]. Moreover, the sensitivity of the solid propellant combustion rate to pressure is also a crucial property that impacts the application of solid propellants in solid rocket engines [28]. Consequently, improving the pressure sensitivity of AP's decomposition characteristics becomes an essential technical method for adjusting the pressure sensitivity of solid propellants. Burning velocity of solid propellants is related to the high temperature decomposition (HTD) temperature, apparent activation energy, apparent heat release of AP and other factors [29–31]. Decreasing the HTD temperature while enhancing the apparent heat release during AP pyrolysis is a critical approach to improving the combustion rate. Presently, there are limited reports on additives capable of modifying AP's decomposition characteristics under different pressure conditions. Composite nano-energetic materials incorporate oxidizer and combustion catalyst at nanometer scale, effectively increasing contact area between oxidizer and combustible agent, accelerating redox reaction rate, enhancing heat release, and reducing mechanical and pressure sensitivity [32,33]. Enhancing these properties not only facilitates the expansion of burning rate and enhancement of combustion stability in solid propellant, but also assumes a regulatory role in optimizing combustion performance.

The present study involves the incorporation or doping of oxidant AP into the nano-skeleton structure of CPs to fabricate a range of composite materials, necessitating further investigation into two factors including thermal decomposition mechanism and apparent heat release at pressures ranging from 3.0 MPa to 9.0 MPa, in order to achieve the objective of enhancing the burning rate. The functional coordination polymer is expected to effectively regulate the thermal decomposition process of AP, mitigate its pressure sensitive decomposition characteristics, and address the technical challenges associated with moisture absorption and agglomeration of some ultrafine AP. This development holds significant implications for high burning rate propellants.

## 2. Material and methods

### 2.1. Materials

Ultrafine ammonium perchlorate with a particle size of approximately 1  $\mu\text{m}$  ( $D_{50}$ ) was procured from Tianyuan New Material Technology Co., Ltd.  $\text{Fe}(\text{NO}_3)_3 \cdot 9\text{H}_2\text{O}$  and 2-Methylimidazole (analytically pure) were obtained from Shanghai Aladdin Biochemical Technology Co., Ltd. Other chemicals, including methanol, acetone and dichloromethane (analytically pure) were purchased from

Shanghai Institute of Organic Chemistry. Hydroxy-terminated polybutadiene (HTPB) was utilized as a binder, Toluene diisocyanate (TDI) as the curing agent, Diethyl sebacate (DOS) as the plasticizer, Methyl apoxide (MAPO) as the cross-linking agent, all these chemicals were acquired from Sinopharm Group. All chemicals were used as received unless otherwise noted.

### 2.2. Preparation of powder catalysts Fe5B

The coordination polymers Fe5B were synthesized using the co-precipitation method. A solution of  $\text{Fe}(\text{NO}_3)_3 \cdot 9\text{H}_2\text{O}$  (4.0 g,  $9.9 \times 10^{-3}$  mol) in 30 mL methanol was added to a solution of 2-methylimidazole (5.0 g,  $5.2 \times 10^{-2}$  mol) in 30.0 mL methanol. The resulting solid mixture was dissolved and continuously stirred for 10 min in a 100-mL beaker at room temperature. During the stirring process, the solution was treated with an addition of 1.0 mL of a NaOH solution (1.0 mol/L). After removing the mother liquor from the mixture, the powder was washed with methanol ( $3 \times 10.0$  mL) and dried in air for two days at room temperature.

### 2.3. Preparation of Fe5B/AP energetic composites

The energetic composite materials were synthesized via a solvent-nonsolvent approach and fabricated by applying a coating of ultrafine AP onto Fe5B at different mass ratios, including 3: 1, 1: 1, 1: 3, 1: 6, 1: 9, 1: 12, and 1: 15. Acetone and dichloromethane were employed as the solvent and nonsolvent respectively. For the mass ratio of 1 to 9, a dispersion was prepared by dispersing 0.1 g of as-prepared Fe5B in 200.0 mL of dichloromethane using an ultrasonic probe homogenizer (Ultrasonic horn size: Ø10; Power: 200 W; Frequency: 20 kHz). A saturated solution of ultrafine AP in acetone was prepared by dissolving 0.9 g of ultrafine AP in 100.0 mL of acetone. Subsequently, the Fe5B powder was added to the ultrafine AP solution under vigorous stirring for a duration of thirty minutes at room temperature with a rotating speed of 600r/min. The resulting Fe5B/AP nanocomposite was filtered and dried at room temperature. The weight ratio of Fe5B: AP was 1: 9. In contrast, a simple mixture consisting of Fe5B (0.10 g) and ultrafine AP (0.90 g) was referred to as Fe5B + AP (1: 9). The preparation process of other proportions of composites followed a similar procedure as described above.

### 2.4. Characterization

The morphology of the as-synthesized composite materials was characterized via scanning electron microscopy (SEM, TESCAN MIRA LMS). Energy Dispersive X-ray Spectrometry (EDAX) was used to analyze the compositions of prepared Fe5B. The crystal structure data were acquired through X-ray diffraction (XRD, Bruker D8 Advance) with Cu-K $\alpha$  radiation, covering a  $2\theta$  range of 5° – 90°. Attenuated total reflection-Fourier transform infrared spectroscopy (ATR-FTIR, PerkinElmer Spectrum 3) was employed to examine the vibrational modes in the wavenumbers range of 4000  $\text{cm}^{-1}$  – 500  $\text{cm}^{-1}$ . Surface chemical component analysis of the materials was conducted via X-ray photoelectron spectroscopy (XPS, Thermo Scientific K-Alpha). The normal pressure (1 atm) simultaneous thermal analysis of the prepared samples was carried out on the thermal gravimetric, coupled with differential scanning calorimeter (TG-DSC, Beijing Henven Scientific Instrument Factory) at a heating rate of 10 °C/min, with a nitrogen gas purged at 40 mL/min. The weight of a sample used in TG measurement was controlled to be  $3 \pm 0.5$  mg with an open alumina crucible. The Brunauer-Emmett-Teller (BET) surface area was performed by physisorption of  $\text{N}_2$  at 77 K using Micromeritics 3Flex Surface Area and Porosity Analyzer. The analysis and detection of the

chemical composition of substances were conducted using Ion Chromatography (IC, ThermoFisher ICS 5000 + ).

## 2.5. Preparation of propellants

In the classic recipe described above, all ingredients were dried at 70 °C for two hours to remove moisture prior to use (Table 1). The ammonium perchlorate ranging from 210 µm to 354 µm accounted for 41 %, while those ranging from 125 µm to 147 µm accounted for 21 %. When formulating propellants with Fe5B/AP, in order to ensure that the overall AP content is 62 %, the AP contained in the burning rate catalysts have been subtracted from the total AP content. The ammonium perchlorate, HTPB, and combustion modifier were mixed for one hour before adding TDI into the propellant mix. After another half an hour of mixing, the final propellant mixture was obtained. To ensure proper curing and mechanical strength development, the propellant slurry was kept at 70 ± 0.5 °C for seven days in a thermostat. Samples were then cooled to room temperature and stored in a desiccator before measurement to avoid moisture absorption. Processing conditions such as mixing temperature, time, level of vacuum applied etc., remained consistent across all sample preparations.

## 2.6. Combustion characteristic study

The burning rates of the samples were measured in an optical pressure vessel with viewing windows for optical testing, as schematically illustrated in Fig. 1. The chamber pressure was monitored using a PT301CS static pressure transducer connected to a data acquisition system. The sample ignition was initiated by igniting a booster placed through the top of the sample. A wide range of pressures, varying from 3.0 MPa to 9.0 MPa, was selected and nitrogen gas was employed for pressurizing the vessel. The combustion flame was captured using a high-speed camera (NX3-S3, Integrated Design Tool, Inc.) to observe flame structure and determine burning rates based on temporal changes in the positions of the burning surface.

The timing began when the top surface of the propellant strip burned completely, and stopped when the combustion process was complete. The pixel position corresponding to the lowest point of the burning surface in a frame is defined as the position of the burning surface, and the burning rate of a sample is calculated as:

$$r_p = \frac{(X_1 - X_0) \times l}{f \times N} \quad (1)$$

where,  $r_p$  is the burning rate, mm/s;  $l$  is the height of one pixel, which is the height of the sample devided by the number of pixels in the initial frame;  $f$  is the frame rate;  $X_1$  and  $X_2$  are the position of burning surface in the two frames; and  $N$  is the frame number between the two frames. The value of a data in this work is the average value of three samples for the accuracy of the burning rate measurement. Furthermore, the pressure exponent of the propellant were determined using the Saint-Robert formula  $r_p = a \cdot p^n$ , where 'a' represents the burning rate coefficient.

## 3. Results and discussion

### 3.1. Characterization of Fe5B/AP energetic composites

Multiple characterization techniques, including XRD, SEM, FTIR, XPS and IC, were employed to analyze the functionalized interface formed by Fe5B and Fe5B/AP composites. The Fe5B failed to locate an exact matching card, and could only gained a rudimentary understanding of its composition and structure (Fig. 2). The characteristic peaks at  $2\theta = 17.92^\circ, 18.26^\circ, 25.72^\circ, 26.48^\circ, 27.64^\circ, 29.30^\circ$ ,

$30.26^\circ$  and  $32.52^\circ$ , corresponding to the main peaks of  $C_{10}H_{10}FeN_8O_6$  (PDF number: 1511774). XRD diffractogram displayed sharp peaks ( $23.54^\circ, 33.61^\circ$ ) that matched with characteristic peaks of  $4Fe(OH)_3 \bullet H_2O$  (PDF number: 461436). XRD diffractogram of unreacted raw material also exhibited clear sharp peaks ( $14.26^\circ, 17.85^\circ, 21.80^\circ, 23.32^\circ, 26.22^\circ$ ) that matched with characteristic peaks of 2-methylimidazole (PDF number: 361686).

The XRD patterns of Fe5B and Fe5B (1: 9) in Fig. 3a confirmed the successful coating of ultrafine AP on Fe5B. The sharp characteristic peaks of Fe5B indicated a high degree of local crystallization order and small particle size. However, the other diffraction peaks were wide, weak, and lack sharpness, suggesting poor crystallinity consistent with previous reports [34]. The XRD characteristic peaks of Fe5B/AP particles at  $15.5^\circ, 19.6^\circ, 22.9^\circ, 24.1^\circ, 24.9^\circ, 30.3^\circ$  and  $34.7^\circ$  closely matched those of the AP raw materials, indicating that the addition of Fe5B would not affect the AP crystal. The XRD patterns of Fe5B/AP (1: 9) and Fe5B + AP (1: 9) exhibited remarkable similarity, thereby indicating the successful modification of AP through both preparation methods. The Fe5B (3: 1) and Fe5B (9: 1) samples exhibited similar characteristics, as evidenced by the presence of the AP characteristic peak in Fig. 3b. With the increase in Fe5B content, at a mass ratio of 15:1, the distinct characteristic peak of Fe5B became evident while the characteristic peak of AP diminished, indicating that ultrasonic treatment only caused surface damage to Fe5B without affecting its crystal structure. In summary, comparable characteristic peaks were observed between functional AP and pure AP, indicating the absence of any phase transition during sample preparation.

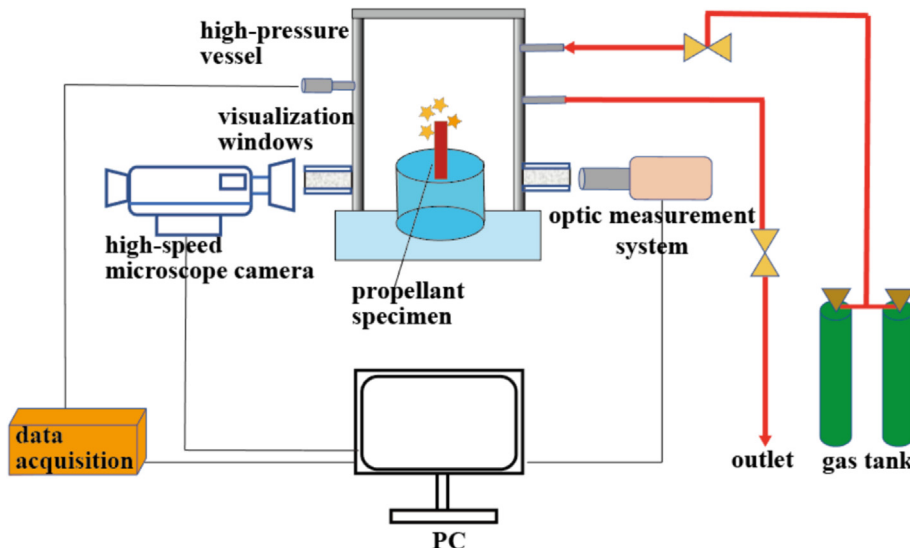
The morphology of the as-synthesized powder was investigated before and after coating using SEM analysis (Fig. 4a and Fig. 5a). Prior to coating, the particles exhibited irregular block shapes with an uneven size distribution, along with numerous small pores and slits of varying sizes on their surfaces. The density distribution of these particles also showed discrepancies, which could be attributed to the synthesis conditions and ligand–metal coordination modes. Following coating, Fe5B displayed a coral-like appearance, with its surface and interior uniformly dispersed with ultrafine AP and the average size of Fe5B/AP particles was approximately 1 µm. The chemical composition of Fe5B and Fe5B/AP particles was confirmed through EDAX analysis, validating their purity (Fig. 4b and Fig. A1). Elemental mapping revealed a homogeneous distribution of Fe, N and O elements within the coordination polymers structure of Fe5B, confirming the successful synthesis of Fe-based CPs. Similarly, EDAX analysis of Fe5B/AP demonstrated a uniform distribution of Fe, N, O and Cl elements (Fig. 5b and Fig. A2), indicating precise chemical composition without any presence of foreign materials. Overall, the solvent-anti solvent technique effectively enables the preparation of Fe5B/AP nanocomposites.

The porous structure of Fe5B was performed by  $N_2$  adsorption/desorption after the samples were heated to 80°C for 12 h in vacuum, and the adsorbed solvent  $CH_3OH$  and water were removed. The  $N_2$  adsorption/desorption isotherms and pore size distribution curves at 77 K are shown in Fig. 6. The Fe5B nanoparticles exhibited characteristic mesoporous structures and conformed to the IV adsorption isotherm. The BET surface area of Fe5B was only  $1.9718 \text{ m}^2/\text{g}$ , while the coated Fe5B had a specific surface area approximately 20 times higher than its original value. The specific surface areas of Fe5B/AP (1: 3) and Fe5B/AP (1: 9) are  $43.4612 \text{ m}^2/\text{g}$  and  $40.2315 \text{ m}^2/\text{g}$  respectively. The pore diameter of Fe5B was 3.44 nm, however, following the application of Fe5B coating, a reduction in pore diameter was observed for both Fe5B/AP (1: 3) and Fe5B/AP (1: 9), resulting in values of 2.89 nm and 2.16 nm respectively. Evidently, AP exhibited a stronger affinity towards the Fe5B surface, leading to an enhanced exposure of catalytically active sites and an increased contact area between active sites and AP crystals.

**Table 1**

Formulation of solid propellants with Fe5B/AP nanoparticles as combustion modifier.

Al/wt%	AP/wt%	DOS/wt%	HTPB-MAPO-TDI/wt%	Combustionmodifier /wt%
18	62	3.6	14.4	2

**Fig. 1.** Diagram of combustion measurement system.

The chemical structure and main functional groups of Fe5B and Fe5B/AP were investigated using FTIR spectroscopy. The strong characteristic peaks observed at 666 and 749 cm<sup>-1</sup> in the as-synthesized Fe5B spectrum were assigned to the stretching vibrations of Fe-O and Fe-N bonds respectively (Fig. 7a). Similarly, the strong characteristic peaks observed at 625 and 677 cm<sup>-1</sup> in the spectrum of Fe5B/AP corresponded to the stretching vibrations of Fe-O and Fe-N bonds individuality [35]. Additionally, the peak observed at 1079 cm<sup>-1</sup> and 1403 cm<sup>-1</sup> can be attributed to the stretching vibration of ClO<sub>4</sub> and the bending vibration peak of NH<sub>4</sub><sup>+</sup> [36], confirming the structural integrity of AP after encapsulation. Furthermore, the characteristic peaks of Fe5B at 3132 cm<sup>-1</sup> and Fe5B/AP (1: 9) at 3310 cm<sup>-1</sup> corresponded to the stretching vibration peaks of -CH<sub>3</sub> on the imidazole ring. The stretching vibration peaks corresponding to the unsaturated C-H bonds on the imidazole ring were observed at 2712 cm<sup>-1</sup> (Fig. 7a) and 2801 cm<sup>-1</sup> (Fig. 7b) respectively. The stretching vibration peaks corresponding to C-N bonds on the imidazole ring were observed at 1297 cm<sup>-1</sup> (Fig. 7a) and 1428 cm<sup>-1</sup> (Fig. 7b) individually. The results provide the evidence that the main framework of Fe5B in the composite material can still be preserved following ultrasonic treatment.

In the Fe 2p spectra of Fe5B nanoparticles (Fig. 8), the peaks at 710.55 eV and 723.96 eV corresponded to Fe 2p<sub>3/2</sub> and Fe 2p<sub>1/2</sub> of Fe<sup>2+</sup> [37]. Simultaneously, the peaks at 712.64 eV and 726.17 eV referred to Fe 2p<sub>3/2</sub> and Fe 2p<sub>1/2</sub> of Fe<sup>3+</sup> [38]. Two satellite peaks (716.99 eV and 729.79 eV) demonstrated the presence of Fe<sup>2+</sup> and another two satellite peaks (720.40 eV and 726.17 eV) confirmed the existence of Fe<sup>3+</sup>. The characteristic peaks of coordination polymers Fe5B, located at 529.78 eV and 399.00 eV, represented the presence of Fe-O and Fe-N in the O 1 s spectra and N 1 s spectra respectively [37,39]. The XPS spectra of Fe5B/AP nanoparticles (1: 9) exhibited the similar characteristic peaks of Fe 2p, N 1 s, O 1 s (Fig. 9 and Fig. A3) as observed for Fe5B particles. The characteristic peaks of Cl 2p, located at 208.17 eV and 209.81 eV, displayed the existence of ClO<sub>4</sub> in Fe5B/AP composite

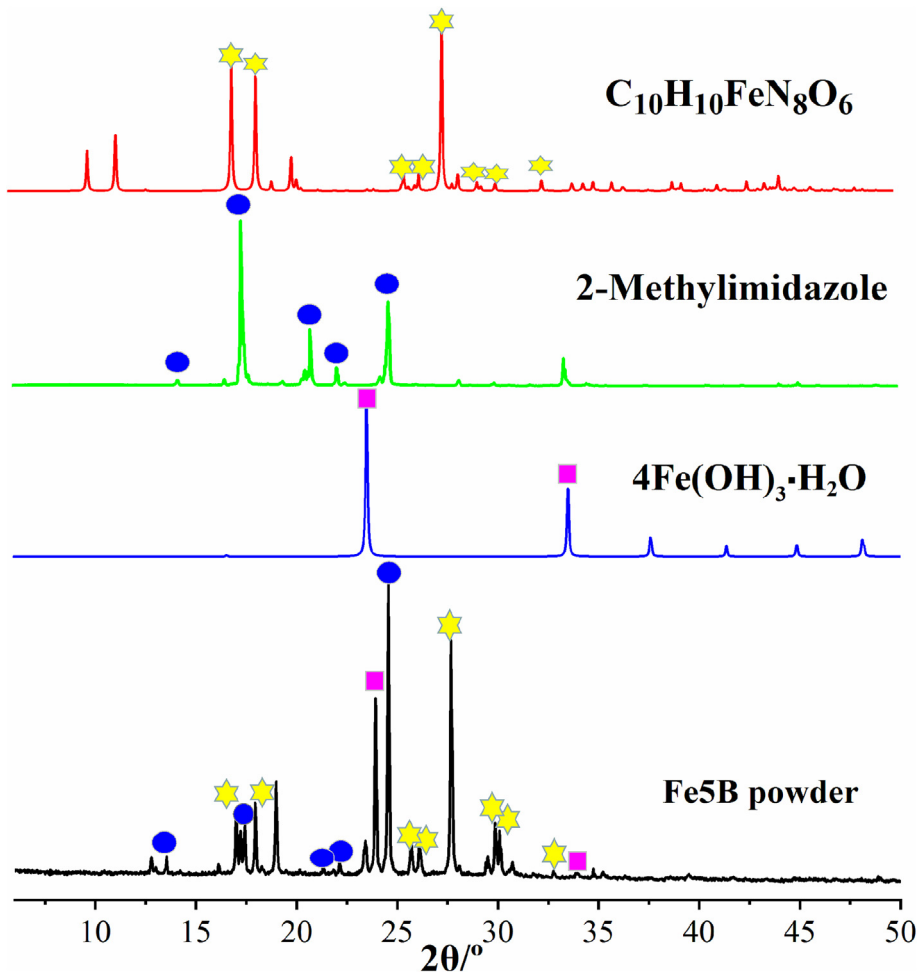
materials [40]. Using Fe5B/AP (3: 1) as a case study, IC analysis revealed that the chloride ion content was 7.70 %, indicating a mass fraction of 25 % for AP in the composite and complete coverage of AP on the Fe5B structure (Fig. A4).

The preserved morphology, structure, and abundant pore structure of the nanocomposites, as well as their large specific surface area, which are conducive to increasing the contact area with AP, enhancing the active sites and improving the catalytic effect. All the results indicate Fe5B/AP particles show promising potential as catalyst candidates for enhancing combustion rates.

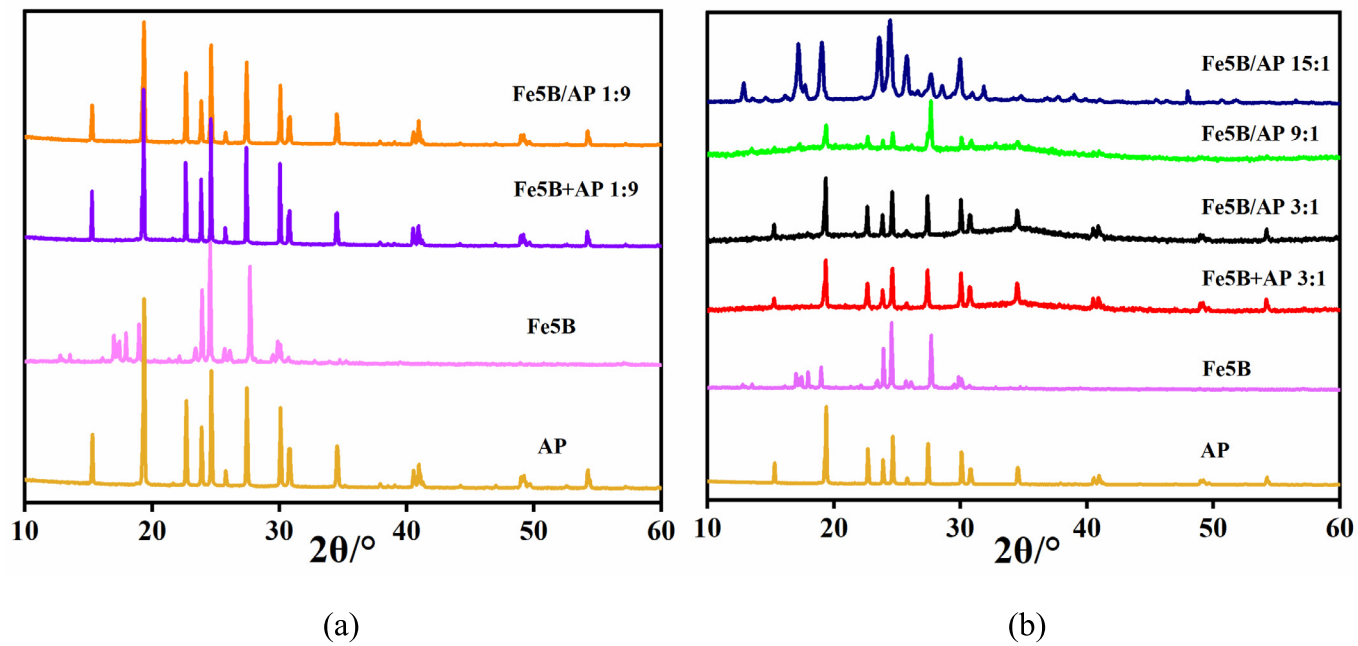
### 3.2. Thermal decomposition analysis of Fe5B/AP energetic composites

Thermal stability plays a critical role in the selection of catalyst materials for solid propellant combustion [22]. The thermal decomposition of pure ammonium perchlorate (AP) and Fe5B/AP nanoparticles was investigated using TG-DSC analysis. For pure AP, an endothermic peak at 245 ± 3 °C was observed, corresponding to the transformation from orthorhombic to cubic crystal form [41]. An exothermic decomposition peak occurred at 301 ± 5 °C due to low temperature decomposition (LTD), followed by a high temperature decomposition (HTD) peak at 453 ± 5 °C [42]. During the LTD stage, partial decomposition reactions could occur with the release of oxidizing species such as HClO<sub>4</sub> and fuel species such as NH<sub>3</sub>. Most NH<sub>3</sub> molecules would adhere to the surface of AP, inhibiting further decomposition. At the HTD peak, NH<sub>3</sub> could desorb from the surface along with complete AP decomposition [43].

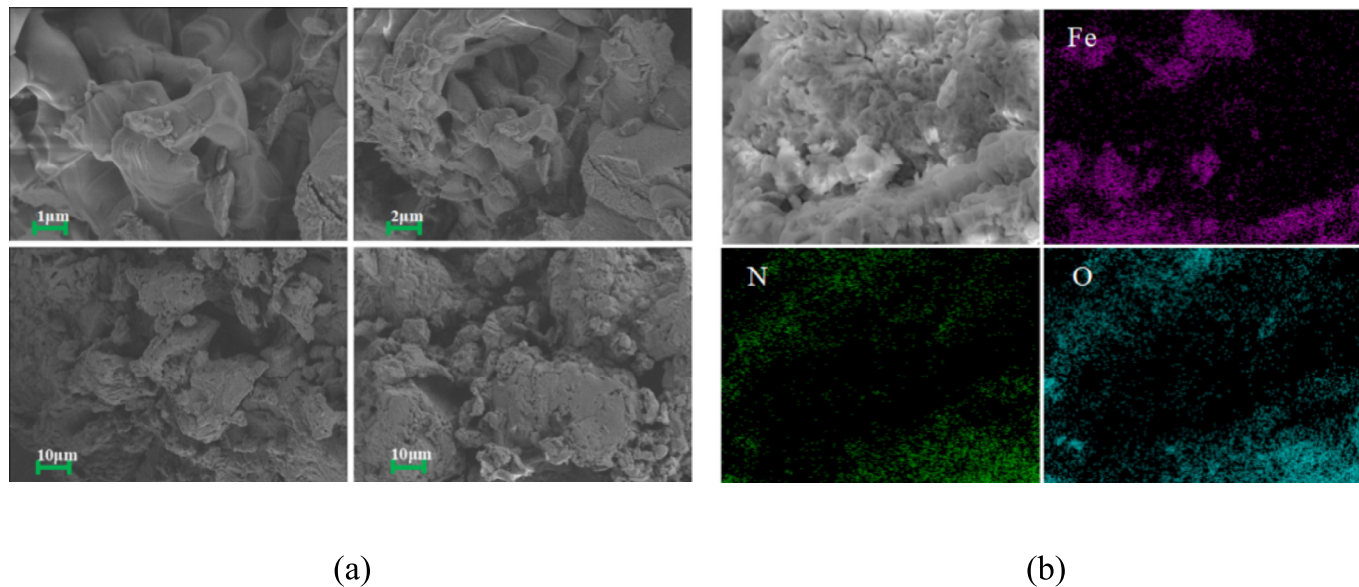
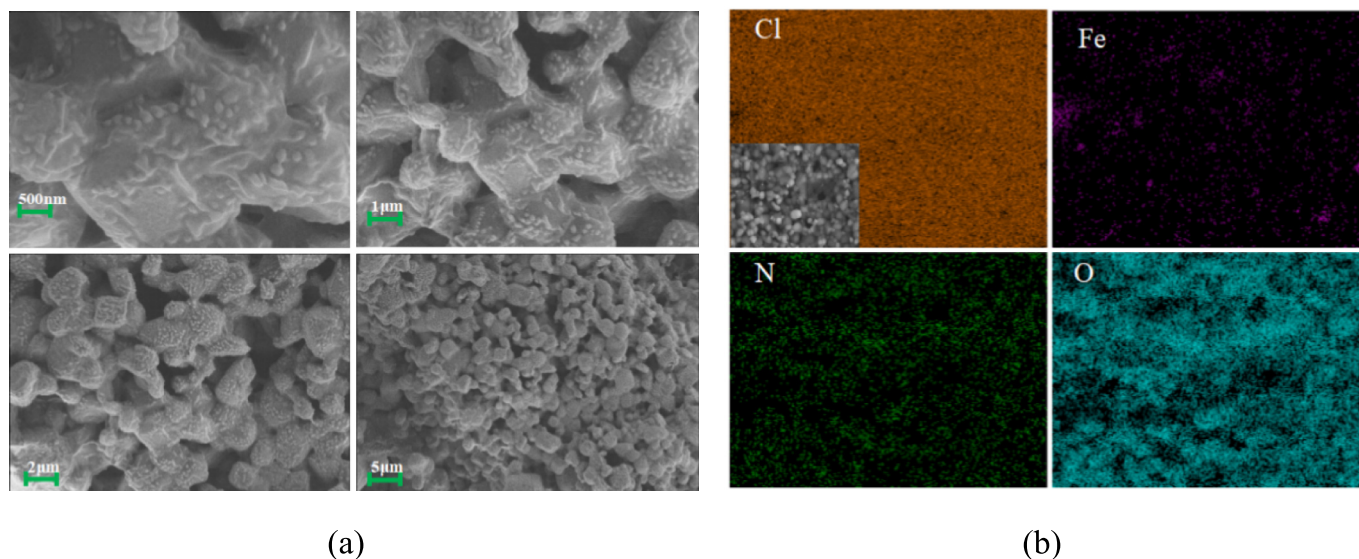
The addition of Fe5B significantly altered the characteristic peaks of AP's thermal decomposition, as evidenced by the DSC curves (Fig. 10). The HTD peak temperature for all eight catalysts decreased from 344.0 °C to 272.1 °C, while the LTD peak remained essentially unchanged. Among them, Fe5B/AP (3: 1) and Fe5B/AP (1: 1) exhibited a significant impact, leading to a noteworthy reduction in the peak temperature of HTD to 272.1 °C and 288.3 °C respectively. This phenomenon may be attributed to the Fe5B adsorption of NH<sub>3</sub> generated during low-temperature decomposi-



**Fig. 2.** The analysis of powder X-ray patterns from Fe5B.



**Fig. 3.** Powder X-ray patterns from Fe5B/AP and Fe5B + AP.

**Fig. 4.** SEM and EDAX images of Fe5B.**Fig. 5.** SEM and EDAX images of Fe5B/AP (1: 9).

tion. Simultaneously, the rapid self-decomposition of Fe5B disrupted the NH<sub>3</sub> structure, thereby facilitating the generation of NO, NO<sub>2</sub>, and N<sub>2</sub>O products that resulted in a significant reduction in the high-temperature decomposition peak of AP as evidenced by a continuous thermal decomposition process[44]. It can be observed that Fe5B/AP catalysts primarily exhibited catalytic effects during the HTD stage of AP, similar to most combustion catalysts [45,46]. Notably, for Fe5B/AP (1: 3), there existed only a 15 °C difference between LTD peak and HTD peak temperatures, with modifiers reducing the HTD peak temperature of AP by 155.7 °C.

The weight-loss temperature range of AP was shortened to 263 °C – 283 °C (3: 1), 268 °C – 300 °C (1: 1), 267 °C – 314 °C (1: 3), 271 °C – 333 °C (1: 6), 272 °C – 338 °C (1: 9), 278 °C–351 °C (1: 12) and 281 °C–355 °C (1: 15) respectively, under the catalysis of Fe5B as illustrated in Fig. 11a. Within the temperature range of 30 °C to 750 °C, two distinct weight-loss processes were observed when varying the Fe5B: AP ratio from a value of 1: 3 to 1: 15, while only one weight loss step was observed for Fe5B: AP ratios of 3: 1 and 1:

1, which was consistent with the DSC results shown in Fig. 11b. Table 2 showed that the high temperature decomposition behavior of AP underwent significant changes upon incorporation with Fe5B nanoparticles, resulting in a substantial increase in total exothermicity. Particularly noteworthy is that the heat release of composites was 1.5 to 3.5 times of pure AP during the high-temperature decomposition stage, indicating a remarkable promoting effect on thermal decomposition by Fe5B/AP nanoparticles. The thermogravimetric analysis revealed that the Fe5B particles individually exhibited a weight loss of only 10 %. However, when combined with AP, there was a significant decrease in the residue rate as the AP content increased, indicating reduced deposition on the surface of the combustion chamber.

The thermal decomposition of Fe5B + AP was also investigated using TG-DSC, revealing significant alterations in the characteristic peaks compared to those observed for Fe5B/AP particles (Fig. 12 and Fig. A5) The LTD stages of Fe5B + AP were found to be 9 °C to 26 °C lower than those of Fe5B/AP particles when transitioning

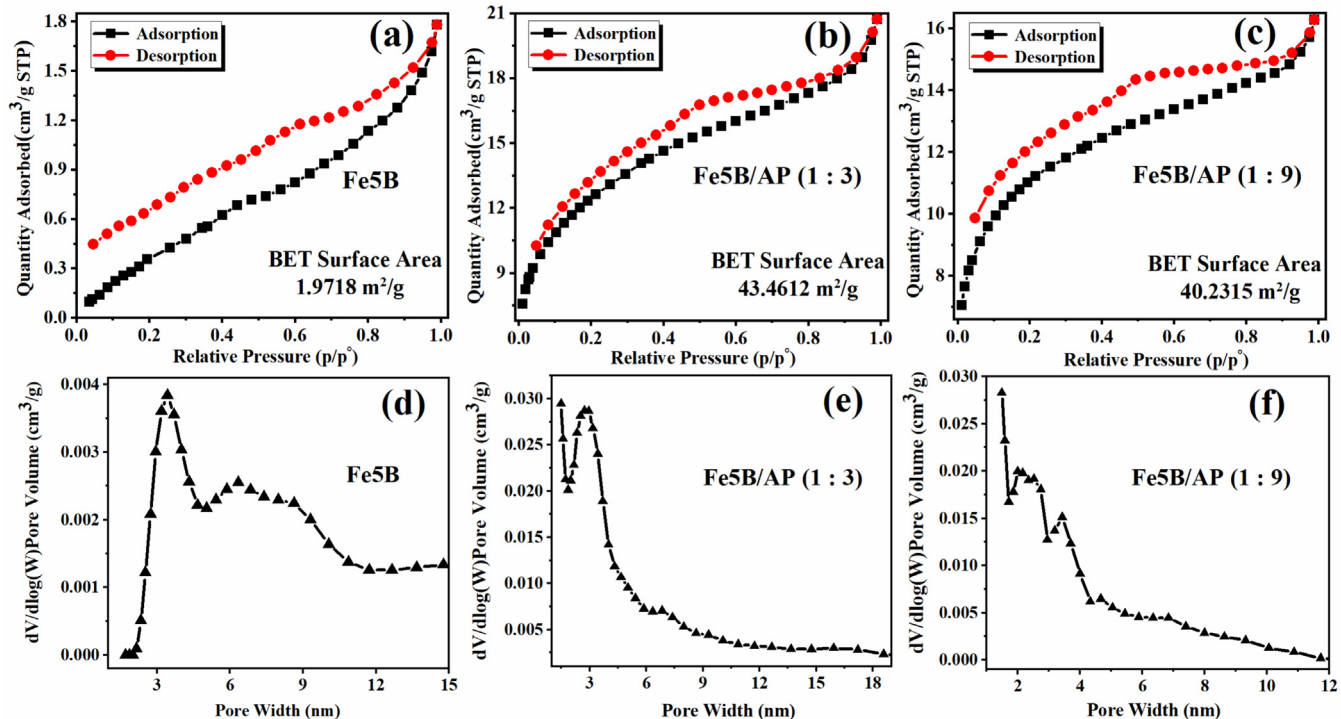


**Fig. 6.** N<sub>2</sub> adsorption/desorption isotherms and pore-size distributions of nanocomposites.

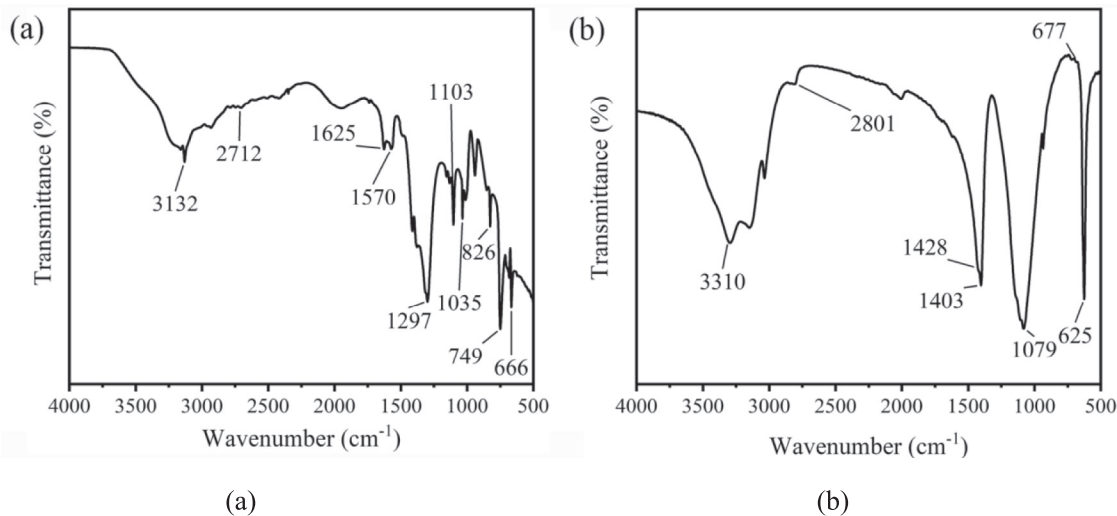


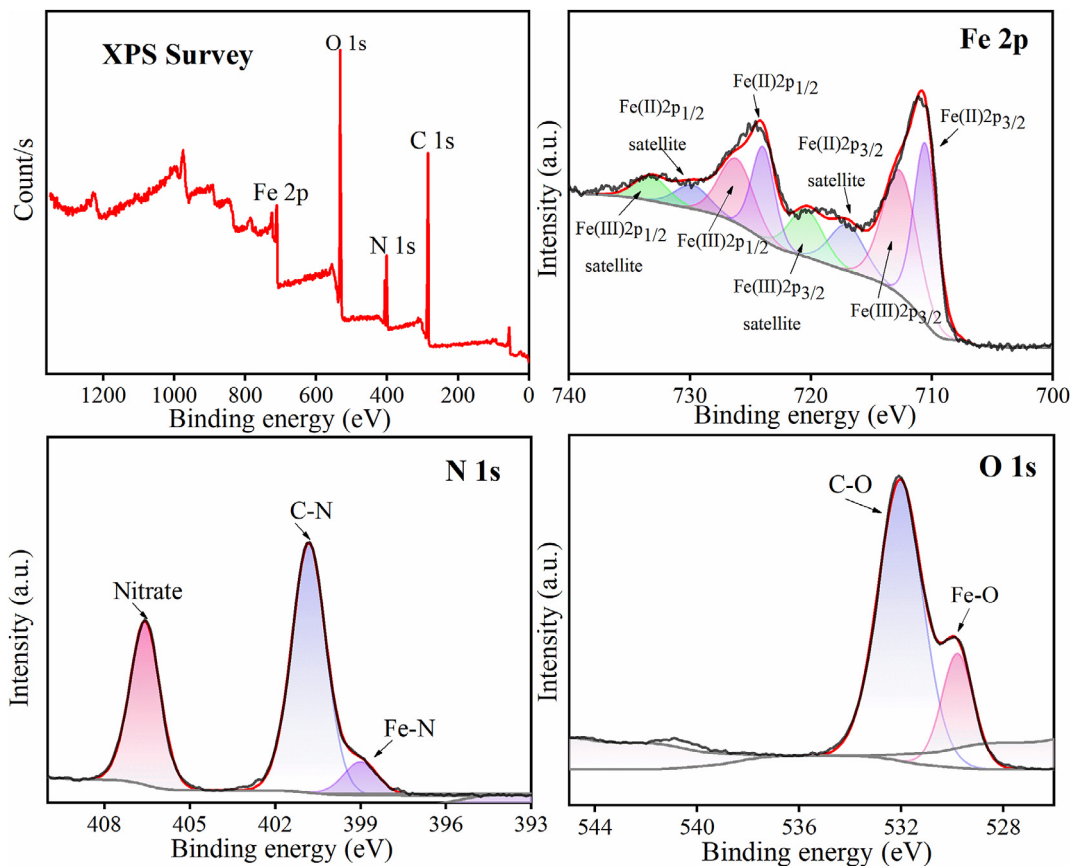
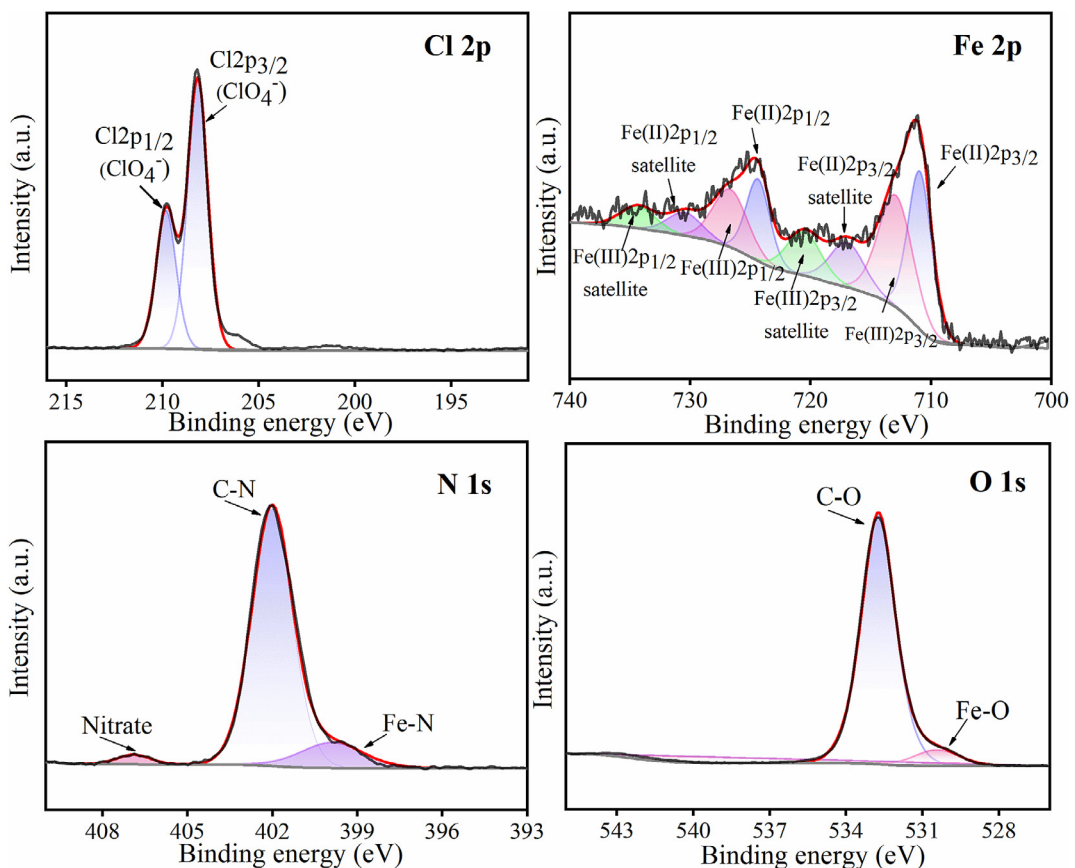
**Fig. 7.** FTIR spectra of Fe5B and Fe5B/AP (1: 9).

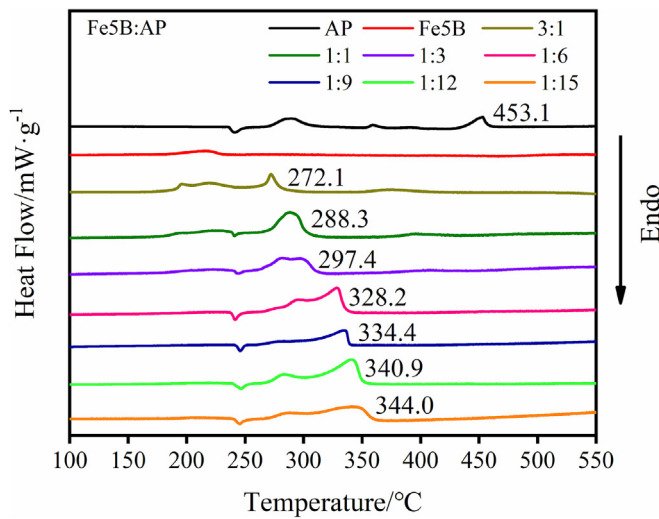
from Fe5B: AP = 3: 1 to Fe5B: AP = 1: 15. Additionally, the HTD peaks of Fe5B + AP were observed to be higher by approximately 8 °C to 19 °C compared with those detected for Fe5B/AP energetic composites. Consequently, it can be concluded that the heat release of Fe5B/AP is more concentrated at lower temperature, thereby promoting combustion.

The positive influence of Fe5B on the solid propellant was further verified by comparing a propellant containing 2 wt% Fe5B particles with a blank sample using TG-DSC curves (Fig. 13). From the DSC curves, it can be observed that the HTD peak of the propellant containing 2 wt% Fe5B was reduced by 41.78 °C compared to the

blank sample (388.44 °C vs 430.22 °C), and the peak intensity was significantly higher than that of the blank sample. The TG curves reveal that while the initial weight loss temperature of both samples remained similar, there was an earlier onset of the second weight loss in the propellant containing 2 wt% Fe5B compared to the blank sample (365.0 °C vs 413.3 °C). Furthermore, it is worth noting that solid propellants incorporating Fe5B nanoparticles exhibited a higher residue ratio than their corresponding blanks due to metal oxides formed from catalysts.

The Fe-based structural units and active metal centers in Fe5B/AP particles play a crucial role as efficient intermediates for elec-

**Fig. 8.** XPS spectra of Fe5B.**Fig. 9.** XPS spectra of Fe5B/AP (1: 9).

**Fig. 10.** DSC curves of pure AP and Fe5B/AP.

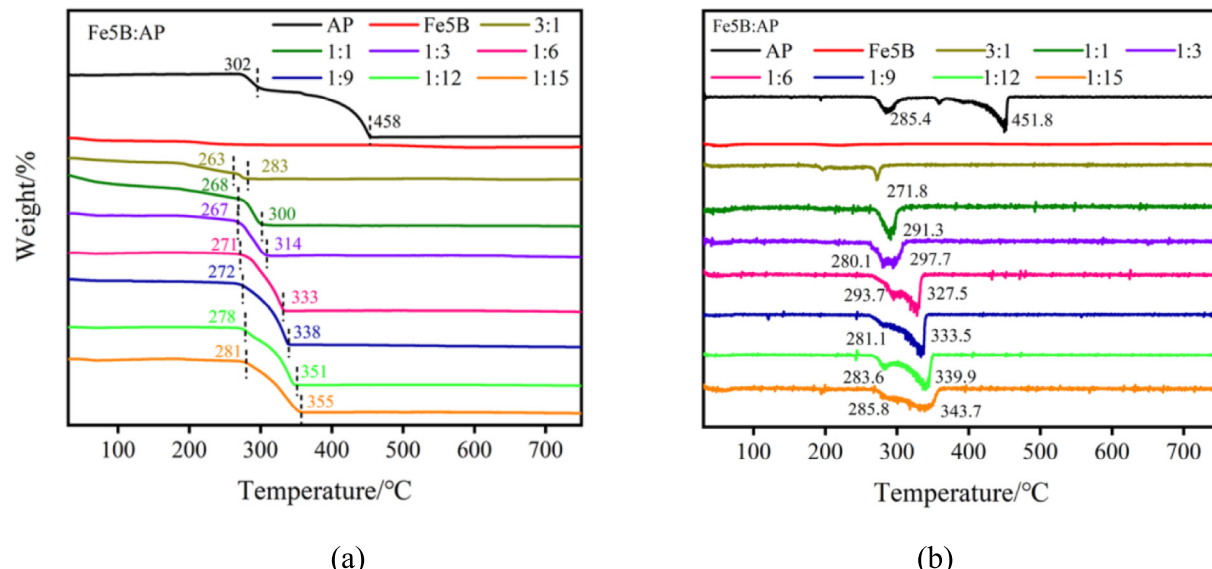
tron transfer [47], thereby enhancing the electron transfer capability, expediting the rates of electron transfer between  $\text{ClO}_4^-$  and  $\text{NH}_4^+$  in the LTD process, and accelerating the electron transfer between

$\text{O}_2$  and  $\text{O}_2^-$  during the HTD stage. Furthermore, the incorporation of Fe5B leads to a reduction in the HTD stage and peak temperature of the first and second weightless platforms compared to pure AP. The utilization of Fe5B/AP energetic composites capitalizes on their unique structural advantages by exposing a greater number of catalytic active sites in nanomaterials, effectively adsorbing more decomposition products, releasing higher heat at lower temperatures, and exhibiting enhanced catalytic performance for solid propellants.

### 3.3. Study on the burning rate with Fe5B/AP nanocomposites

To gain a clearer understanding of the impact of different combustion modifiers, **Table 3** presented a comparison of the burning rates for AP-HTPB propellant with varying ratios of combustion catalysts.

As presented in **Table 3** and **Fig. 14**, the virgin propellant with a 62 % oxidizer loading exhibited burning rates ranging from 3.661 mm/s to 7.710 mm/s at pressure ranges of 3.0 MPa, 5.0 MPa, 6.0 MPa, 7.0 MPa, and 9.0 MPa. In case of the solid propellants with combustion modifiers, higher burning rates were observed to varying degrees. The burning rates had been found in order of 6.020 mm/s to 10.726 mm/s for 2 wt% Fe5B loading, and 5.530 mm/s to 9.040 mm/s for 2 wt% Fe5B/AP (3: 1) loading at similar pressure ranges. For regulators affecting burning rate at a weight percentage of 2 wt%, the propellants containing Fe5B/

**Fig. 11.** TG-DTG curves of pure AP and Fe5B/AP.**Table 2**

Peak temperatures and net exothermicity of propellants with Fe5B/AP nanoparticles.

Types of propellant	Endothermic peak temperature [°C]	Exothermic peak temperature [°C]		Net Exothermicity [J/g]		Weight-loss ratio/%	
		Low	High	Low(-)	High(-)	First platform	Second platform
AP	239.2	288.6	453.1	298.2	390.2	20	90
Fe5B	—	—	—	227.4	—	5	10
Fe5B/AP (3: 1)	—	196.5	272.1	378.53	619.42	22	30
Fe5B/AP (1: 1)	240.0	—	288.3	—	1102.4	43	80
Fe5B/AP (1: 3)	243.6	278.8	297.4	647.0	1066.04	13	62
Fe5B/AP (1: 6)	239.2	294.7	328.8	646.0	1168.3	7	85
Fe5B/AP (1: 9)	245.0	281.1	334.4	197.5	844.7	9	95.8
Fe5B/AP (1: 12)	242.3	282.8	340.9	539.8	1373.0	1	85
Fe5B/AP (1: 15)	242.2	285.3	344.0	472.4	1068.5	3	77

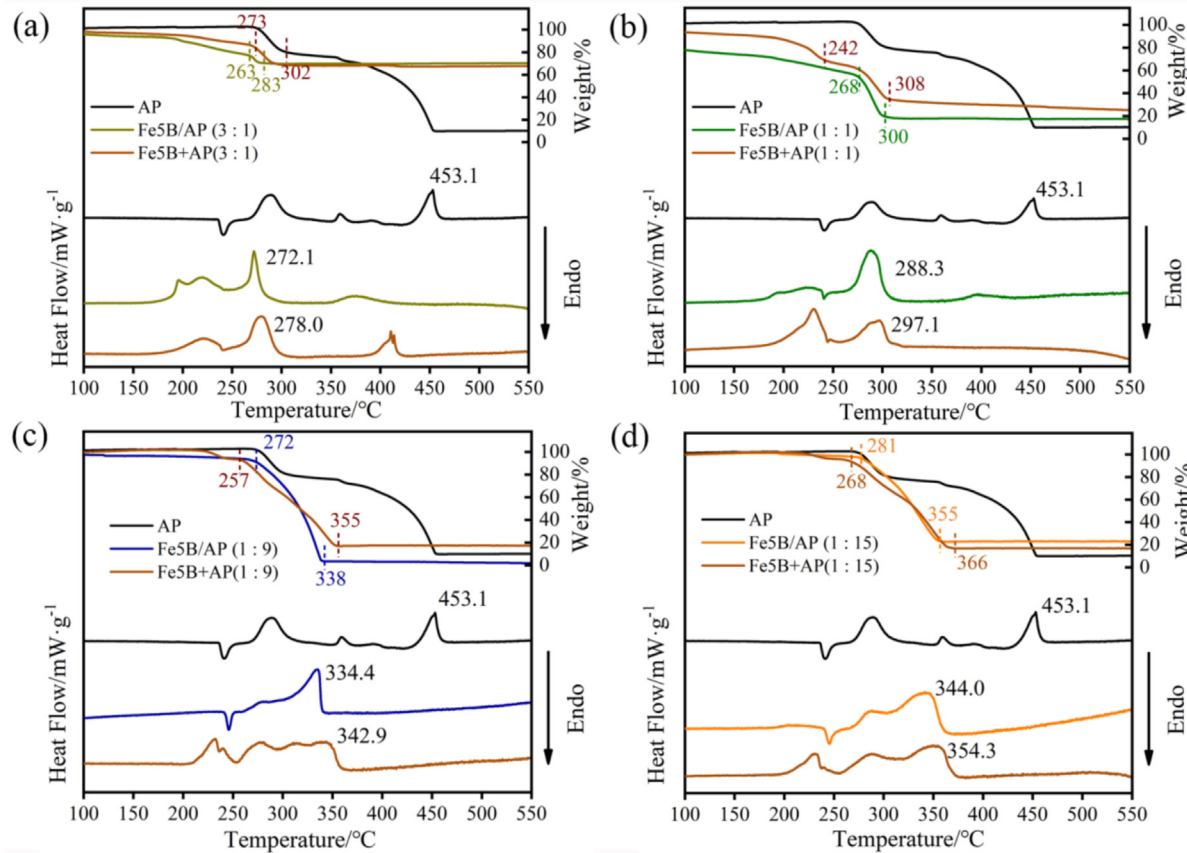


Fig. 12. Comparison of TG-DSC curves of Fe5B + AP and Fe5B/AP 3: 1 (b) 1: 1 (c) 1: 9 (d) 1: 15.

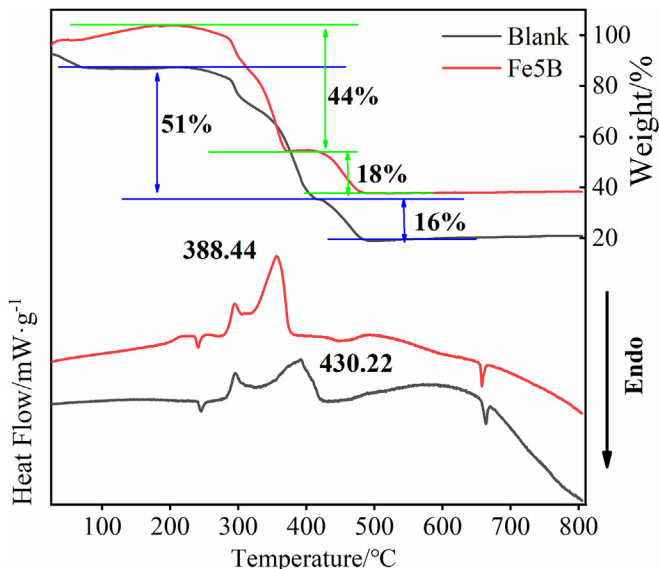


Fig. 13. Comparison of TG-DSC curves of the solid propellant with and without Fe5B particles.

AP (1: 1) and Fe5B/AP (1: 9) exhibited respective burning velocities ranging from 5.191 mm/s to 8.731 mm/s and 4.253 mm/s to 7.047 mm/s. These values were higher than those observed for virgin propellant under similar pressure conditions but had lower pressure index values. It is worth mentioning that among the series

using Fe5B as an additive, the best performing solid propellant exhibited burning velocity ranging from 6.310 mm/s to 10.390 mm/s when loaded with 2 wt% Fe5B/AP (1: 3) within the pressure ranges from 3.0 MPa to 9.0 MPa. Compared to blank samples, the burning velocity of the solid propellant with a Fe5B/AP (1: 3) ratio was enhanced by 42 % at 3.0 MPa, 37 % at 6.0 MPa, and 26 % at 9.0 MPa. The observed phenomenon can be attributed to the optimal dispersion ratio of Fe5B and AP, ensuring a homogeneous distribution of AP on the surface of Fe5B. This phenomenon prevents excessive doping of Fe5B, which could impede the release of reaction heat, and excessive aggregation of ultra-fine AP particles that would have an adverse impact on the combustion performance of Fe5B/AP particles. In comparison, for a loading of 2 wt%  $\text{Fe}_2\text{O}_3$ , burning rates ranged from 5.772 mm/s to 11.319 mm/s were found. The propellant with a Fe5B/AP (1: 3) ratio exhibited superior burning rate compared to commercially available  $\text{Fe}_2\text{O}_3$  and showed a significant increase in burning rate by approximately 10 % under low pressure conditions. Although the combustion rate of propellant with Fe5B/AP (1: 3) under high pressure was not as good as that of  $\text{Fe}_2\text{O}_3$ , the concentration of Fe5B in the propellant was merely one-quarter that of the propellants with  $\text{Fe}_2\text{O}_3$ . Importantly, the pressure exponent was much lower than the propellant with  $\text{Fe}_2\text{O}_3$ .

With the increasing Fe5B loading, the pressure index values exhibited a decreasing trend, providing evidence that Fe5B/AP nanocomposites can mitigate the sensitivity of the burning process to pressure. The pressure index values of propellant with Fe5B/AP (1: 3) and Fe5B/AP (3: 1) loading were merely 0.456 and 0.422, and far less than that of propellant with commercial iron oxide (0.625). Notably, the combustion behavior of propellant incorporating Fe5B/AP particles demonstrated remarkable superiority.

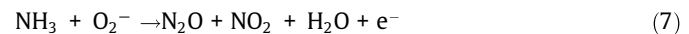
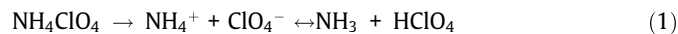
**Table 3**

Burning rate of AP-HTPB propellants with different combustion catalysts.

Combustion catalysts	Burning rate ( $r_p$ )/ mm·s <sup>-1</sup>						Pressure exponent ( $n$ )
	3.0 MPa	5.0 MPa	6.0 MPa	7.0 MPa	9.0 MPa	$R^2$	
Blank	3.661	5.132	5.299	6.179	7.710	0.96784	0.654
Fe5B	6.020	7.547	8.094	9.115	10.726	0.97584	0.517
Fe5B/AP(3: 1)	5.530	6.514	6.700	7.515	9.040	0.93399	0.422
Fe5B/AP(1: 1)	5.191	6.515	7.566	7.812	8.731	0.98155	0.483
<b>Fe5B/AP(1: 3)</b>	<b>6.310</b>	<b>7.546</b>	<b>8.342</b>	<b>9.152</b>	<b>10.390</b>	0.97981	<b>0.456</b>
Fe5B/AP(1: 9)	4.253	5.120	5.773	6.450	7.047	0.97538	0.476
Fe <sub>2</sub> O <sub>3</sub>	5.772	8.354	9.388	10.203	11.319	0.98150	0.625

### 3.4. Catalytic mechanism

The thermal decomposition of AP is a complex multiphase process, and the complete mechanism of AP's thermal decay has not yet been fully understood. According to the widely recognized proton transfer mechanism [48], both the LTD and HTD stages involve the decomposition process of AP into NH<sub>3</sub> and HClO<sub>4</sub>, followed by further reoxidation and reduction reactions leading to the formation of HCl, H<sub>2</sub>O and other gaseous products. Intermediate products, such as O<sub>2</sub>, NO, N<sub>2</sub>O, are generated through ClO<sub>3</sub> accepting electrons to form ClO<sub>3</sub><sup>-</sup>, which then react with NH<sub>3</sub> in a typical solid–gas two-phase reaction as described by Eqs. (1) – (5). The crucial step in the HTD stage involves the conversion of O<sub>2</sub> to O<sub>2</sub><sup>-</sup>. These superoxide anions, along with other products generated by HClO<sub>4</sub>, facilitate NH<sub>3</sub> decomposition and ultimately drive the thermal decomposition of AP towards N<sub>2</sub>O, NO<sub>2</sub> and H<sub>2</sub>O (Eqs. (6) and (7)) [49]. However, during the LTD stage, complete decomposition of AP is hindered due to NH<sub>3</sub> adsorption on its surface. Meanwhile, the residual solid AP undergoes further decomposition at high temperatures, leading to the full activation of NH<sub>3</sub> and HClO<sub>4</sub> adsorbed around AP and resulting in the generation of volatile substances [43].



The Fe5B/AP composites exhibit a large specific surface area, pore volume, and abundant catalytic sites, enabling efficient absorption and enrichment of NH<sub>3</sub> and HClO<sub>4</sub> gases while restricting their reaction space. Under the influence of gaseous products [50], coordination metal ions undergo transformation into nanoscale metal oxides, which can serve as catalysts for AP decomposition due to their characteristic quasi-conductive nature with hole conduction [51]. Consequently, these in situ generated metal oxides exhibit exceptional catalytic activity attributed to the presence of highly active centers that facilitate the adsorption of various oxygen species acted as electron acceptors, including peroxide ions and oxygen ions, expediting the thermal decomposition of AP's HTD stage [44] (Fig. 15).

Based on the aforementioned results, the presence of Fe5B/AP composites significantly influence the thermal reaction transitions of ammonium perchlorate. The catalytic effect of Fe5B/AP nanoparticles is predominantly observed within the HTD region, distinguished by its distinctive coral-like morphology. This exceptional architecture offers a greater concentration of active sites and promotes improved electron transfer capability, which can be ascribed to the existence of Fe-based entities. Notable changes in exothermic positions are also observed, indicating an accelerated electron process and promoting the thermal decomposition of AP. Although the burning rate characteristics of the propellants with Fe5B/AP was seem like almost the same as that of the propellant with Fe<sub>2</sub>O<sub>3</sub> [44], the content of Fe5B was only 1/4 of Fe<sub>2</sub>O<sub>3</sub> content in the best burning rate formula. Additionally, the pressure index of the propellants with Fe5B/AP (1: 3) was 0.169 lower than those

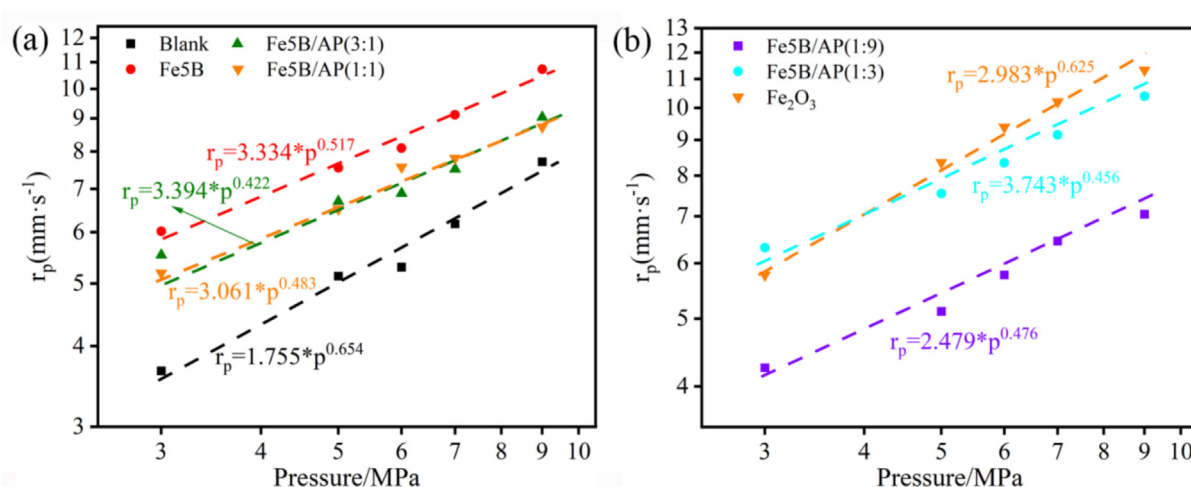
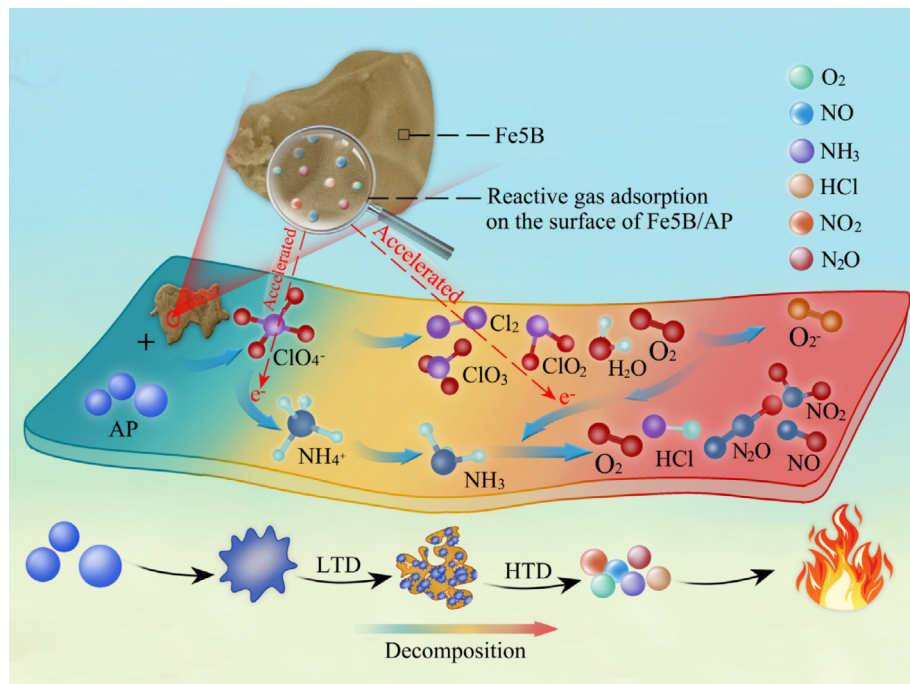


Fig. 14. Comparison of burning rates of virgin AP/HTPB propellants with different combustion catalysts.



**Fig. 15.** Mechanism diagram of AP's decomposition processes catalyzed by Fe5B/AP.

of  $\text{Fe}_2\text{O}_3$ . These results highlight the superior performance of Fe5B as a burning rate catalyst.

#### 4. Conclusion

In summary, a series of energetic composites comprising varying proportions of Fe-based coordination polymers (CPs) were synthesized using the solvent-nonsolvent method to investigate their catalytic properties for the thermal decomposition of ammonium perchlorate. The Fe5B/AP nanocatalysts exhibit distinctive coral-shaped morphology, large specific surface area, excellent thermal stability, strong electron transfer ability inherent in Fe-based structures and active metals, which significantly reduce the HTD peak temperature of ammonium perchlorate and enhance its apparent heat release. Fe5B/AP (1: 3) nanoparticles exhibit superior combustion performance with less amount, achieving a reduced pressure exponent, effectively preventing agglomeration of ultrafine AP particles and enhancing catalytic efficiency while minimizing migration of Fe-based combustion catalysts and sensitivity to pressure. The catalytic mechanism demonstrates that Fe-based structural units and active metal centers of Fe5B/AP particles efficiently serve as intermediates for electron transfer, expediting the rates of electron transfer between  $\text{ClO}_4^-$  and  $\text{NH}_4^+$  in the LTD process. During the HTD stage, the abundant catalytic sites of Fe5B/AP generate iron oxides in situ, facilitating the adsorption of oxygen species during AP's thermal decomposition process and promoting an increase in heat release. Therefore, Fe5B/AP composites hold significant potential as highly efficient and less sensitive catalysts for solid propellants based on ammonium perchlorate.

#### CRediT authorship contribution statement

**Yan Zhao:** Writing – review & editing, Writing – original draft. **Xing Zhou:** Writing – review & editing, Funding acquisition. **Hongfeng Ji:** Investigation. **Bian Li:** Formal analysis. **Wei Zhou:** Formal analysis. **Yao-Hua Liu:** Validation. **Guixi Liu:** Investigation.

#### Funding

This work was supported by the Stabilization Support Project (HTDJ021520240925009), National Natural Science Foundation of China, Joint Fund Project (U22B20138), Independent Innovation Science Fund Project of Natinal University of Defense Technology (23-ZZCX-ZZGC-01-10) and China Postdoctoral Science Foundation (2024 M764285/GZC20233522).

#### Declaration of competing interest

The authors declare that they have no known competing financial interests or personal relationships that could have appeared to influence the work reported in this paper.

#### Appendix A. Supplementary data

Supplementary data to this article can be found online at <https://doi.org/10.1016/j.apt.2025.104865>.

#### References

- [1] D.R. Kshirsagar, S. Jain, S.N. Jawaldar, et al., Evaluation of nano- $\text{Co}_3\text{O}_4$  in HTPB-based composite propellant formulations, Propellants. Explos. Pyrotech. 41 (2016) 304–311. <https://doi.org/10.1002/prep.201500158>.
- [2] C. Zeng, F. Gong, S. Liu, et al., Effect of Al@GAP composite particles on thermal decomposition performance of LLM-105, Chin. J. Explos. Propellants. 40 (2017) 29–35. <https://doi.org/10.14077/j.issn.1007-7812.22017.04.005>.
- [3] W. Pang, L.T. DeLuca, X. Fan, et al., Combustion behavior of AP/HTPB/Al composite propellant containing hydroborate iron compound, Combust. Flame. 220 (2020) 157–167. <https://doi.org/10.1016/j.combustflame.2020.06.037>.
- [4] F. Zhen, X. Zhou, L. Wang, et al., Study on burning and thermal decomposition properties of HTPB propellant containing synthesized micro-nano ferric perfluoroctanoate, propellants, Explos. Pyrotech. 44 (2019) 362–368. <https://doi.org/10.1002/prep.201800309>.
- [5] H. Li, B. Liu, Y. Xu, et al., Tunable catalytic activity of energetic multi-metal hexanitro complexes for RDX decomposition and ignition, J. Anal. Appl. Pyrolysis. 157 (2021) 105228. <https://doi.org/10.1016/j.jaat.2021.105228>.
- [6] D. Ren, M. Wei, J. Shi, et al., Synthesis, crystal structure and catalytic performance of a novel five-coordinated energetic copper(II) compound, Z.

- Anorg. Allg. Chem. 648 (2021) e202100106. <https://doi.org/10.1002/zaac.202100106>.
- [7] J. Shen, Z. Liu, B. Xu, et al., Tuning the thermal, mechanical, and combustion properties of NC-TEGDN-RDX propellants via incorporation of graphene nanoplates, *J. Energ. Mater.* 38 (2020) 326–335. <https://doi.org/10.1080/07370652.2019.1689314>.
- [8] J. Shen, Z. Liu, B. Xu, et al., Influence of carbon nanofibers on thermal and mechanical properties of NC-TEGDN-RDX triple-base gun propellants, *Propellants. Explos. pyrotech.* 44 (2019) 355–361. <https://doi.org/10.1002/prep.201800257>.
- [9] R. Xu, L. Yang, H. Fang, et al., Copper complexes in carbon nanotubes as catalysts for thermal decomposition of energetic oxidizers, *ACS Appl. Nano Mater.* 5 (2022) 14942–14953. <https://doi.org/10.1021/acsnano.2c03191>.
- [10] J. Wang, X. Lian, S. Chen, et al., Effect of Bi<sub>2</sub>WO<sub>6</sub>/g-C<sub>3</sub>N<sub>4</sub> composite on the combustion and catalytic decomposition of energetic materials: an efficient catalyst with g-C<sub>3</sub>N<sub>4</sub> carrier, *J. Colloid Interface Sci.* 610 (2022) 842–853. <https://doi.org/10.1016/j.jcis.2021.11.131>.
- [11] J. Wang, X. Lian, Q. Yan, et al., Unusual Cu-Co/GO composite with special high organic content synthesized by an in situ self-assembly approach: pyrolysis and catalytic decomposition on energetic materials, *ACS Appl. Mater. Interfaces* 12 (2020) 28496–28509. <https://doi.org/10.1021/acsmami.0c05298>.
- [12] W. Pang, L.T. De Luca, X. Fan, et al., Effects of different nano-sized metal oxide catalysts on the properties of composite solid propellants, *Combust. Sci. Technol.* 188 (2016) 315–328. <https://doi.org/10.1080/00102202.2015.1083986>.
- [13] F. Yang, D. Deng, X. Pan, et al., Understanding nano effects in catalysis, *Natl. Sci. Rev.* 2 (2015) 183–201. <https://doi.org/10.1093/nsr/nwv024>.
- [14] J.S.M. Lee, K.I. Otake, S. Kitagawa, Transport properties in porous coordination polymers, *Coord. Chem. Rev.* 421 (2020) 213447. <https://doi.org/10.1016/j.ccr.2020.213447>.
- [15] L. Xu, J. Qiao, S. Xu, et al., Constructing strategies and applications of nitrogen-rich energetic metal-organic framework materials, *Catalysts* 10 (2020) 690. <https://doi.org/10.3390/catal10060690>.
- [16] Z. Wang, C. Lai, L. Qin, et al., ZIF-8-modified MnFe<sub>2</sub>O<sub>4</sub> with high crystallinity and superior photo-Fenton catalytic activity by Zn-O-Fe structure for TC degradation, *Chem. Eng. J.* 392 (2020) 124851. <https://doi.org/10.1016/j.cej.2020.124851>.
- [17] L. Li, W. Yang, Q. Yang, et al., Accelerating chemo and regioselective hydrogenation of alkynes over bimetallic nanoparticles in a metal-organic framework, *ACS Catal.* 10 (2020) 7753–7762. <https://doi.org/10.1021/acscatal.0c00177>.
- [18] T. Jin, Y. Li, W. Jing, et al., Cobalt-based metal organic frameworks: a highly active oxidase-mimicking nanozyme for fluorescence “turn-on” assays of biothiol, *Chem. Commun.* 56 (2020) 659–662. <https://doi.org/10.1039/C9CC06840F>.
- [19] J. Han, C.L. Hill, A coordination network that catalyzes O<sub>2</sub>-based oxidations, *J. Am. Chem. Soc.* 129 (2007) 15094–15095. <https://doi.org/10.1021/ja069319v>.
- [20] F.X. Llabrés i Xamena, O. Casanova, R. Galiasso Tailleur, F. Llabresixamena, H. Garcia, A. Corma, Metal organic frameworks (MOFs) as catalysts: a combination of Cu<sup>2+</sup> and Co<sup>2+</sup> MOFs as an efficient catalyst for tetralin oxidation, *J. Catal.* 255 (2) (2008) 220–227. <https://doi.org/10.1016/j.jcat.2008.02.011>.
- [21] Y. Yang, Y. Bai, F. Zhao, et al., Effects of metal organic frame-work Fe-BTC on the thermal decomposition of ammonium perchlorate, *RSC Adv.* 6 (2016) 67308–67314. <https://doi.org/10.1039/C6RA12634K>.
- [22] J. Yan, H. Wang, B. Jin, et al., Cu-MOF derived Cu/Cu<sub>2</sub>O/C nanocomposites for the efficient thermal decomposition of ammonium perchlorate, *J. Solid State Chem.* 297 (2021) 122060. <https://doi.org/10.1016/j.jssc.2021.122060>.
- [23] S. Lashgari, M. Sharifzadeh Baei, F. Farhadi Abkanar, et al., Catalytic effect of solvothermally prepared Cu<sub>2</sub>(bdc)<sub>2</sub>(bpy) metal-organic framework on thermal decomposition of ammonium perchlorate, *J. Solid State Chem.* 295 (2021). <https://doi.org/10.1016/j.jssc.2020.121940>.
- [24] B. Pierre, D. Dmitry, C. Laurent, A revised model of ammonium perchlorate combustion with detailed kinetics, *Combust. Flame.* 255 (2023) 112891. <https://doi.org/10.1016/j.combust.flame.2023.112891>.
- [25] B. Gou, Y. Kou, Y. Hu, et al., Effect of nano-copper chromite on the thermal decomposition and cmbusion of AP-based solid propellants, *Propell. Explos. Pyrot.* 47 (2022). <https://doi.org/10.1002/prep.202200087>.
- [26] Y. Yan, B. Jin, Q. Zhou, Copper loaded carbon aerogel from chitosan-precursor promotes thermal decomposition of ammonium perchlorate for solid propellants, *Adv. Powder. Technol.* 34 (2023) 104188. <https://doi.org/10.1016/j.apt.2023.104188>.
- [27] L. Zhou, S. Cao, L. Zhang, et al., Promotion of the Co<sub>3</sub>O<sub>4</sub>/TiO<sub>2</sub> interface on catalytic decomposition of ammonium perchlorate, *ACS Appl. Mater. Interfaces* 14 (2022) 3476–3484. <https://doi.org/10.1021/acsmami.1c20510>.
- [28] D. Klinger, A. Casey, T. Manship, et al., Prediction of solid propellant burning rate characteristics using machine learning techniques, *Propell. Explos. Pyrot.* 48 (2023). <https://doi.org/10.1002/prep.202200267>.
- [29] G. Hao, J. Liu, Q. Liu, et al., Facile preparation of AP/Cu(OH)<sub>2</sub> core-shell nanocomposites and its thermal decomposition behavior, *Propell. Explos. Pyrot.* 42 (2017) 947–952. <https://doi.org/10.1002/prep.201600209>.
- [30] Y. Cang, L.P. Wang, Understanding AP/HTPB composite propellant combustion from new perspectives, *Combust. Flame* 259 (2024) 113108. <https://doi.org/10.1016/j.combustflame.2023.113108>.
- [31] C. Dennis, B. Bojko, On the combustion of heterogeneous AP/HTPB composite propellants: a review, *Fuel* 254 (2019) 115646. <https://doi.org/10.1016/j.fuel.2019.115646>.
- [32] S.G. Hosseini, R. Abazari, A. Gavi, Pure CuCr<sub>2</sub>O<sub>4</sub> nanoparticles: synthesis, characterization and their morphological and size effects on the catalytic thermal decomposition of ammonium perchlorate, *Solid State Sci.* 37 (2014) 72–79. <https://doi.org/10.1016/j.solidstatosciences.2014.08.014>.
- [33] S. Chaturvedi, P.N. Dave, N.N. Patel, Thermal decomposition of AP/HTPB propellants in presen-ce of Zn nanoalloys, *Appl. Nanosci.* 5 (2015) 93–98. <https://doi.org/10.1007/s13204-014-0296-3>.
- [34] J. Liu, H. Yu, L. Wang, Superior absorption capacity of tremella like ferrocene based metal-organic framework in removal of organic dye from water, *J. Hazard. Mater.* 392 (2020) 122274. <https://doi.org/10.1016/j.jhazmat.2020.122274>.
- [35] P.R. Griffiths, Fourier transform infrared spectrometry, *Science* 222 (1983) 297–302. <https://doi.org/10.1126/science:6623077>.
- [36] A. Finch, *Chemical applications of far infrared spectroscopy*, Academic Press, New York, 1970.
- [37] M.C. Biesinger, B.P. Payne, A.P. Grosvenor, et al., Resolving surface chemical states in XPS analysis of first row transition metals, oxides and hydroxides: Cr, Mn, Fe, Co and Ni, *Appl. Surf. Sci.* 257 (2011) 2717–2730. <https://doi.org/10.1016/j.apsusc.2010.10.051>.
- [38] S.G. Hosseini, R. Ahmadi, A. Ghavi, et al., Synthesis and characterization of  $\alpha$ -Fe<sub>2</sub>O<sub>3</sub> mesoporous using SBA-15 silica as template and investigation of its catalytic activity for thermal decomposition of ammonium perchlorate particles, *Powder Technol.* 278 (2015) 316–322. <https://doi.org/10.1016/j.powtec.2015.03.032>.
- [39] X. Kong, Z. Xi, Y. Jiang, et al., Fe-N-C decorated fibrous network-wrapped biomass SiOx/C with gradient conductive structure for high performance Li-ion battery anodes, *Chem. Eng. J.* 477 (2023) 147178. <https://doi.org/10.1016/j.cej.2023.147178>.
- [40] K. Naoi, W.H. Smyrl, XPS studies on conducting polymers: polypyrrole films doped with perchlorate and polymeric anions, *Chem. Mater.* 4 (1992) 988–994. <https://doi.org/10.1021/cm00023a012>.
- [41] J. Wang, Y. Li, H. Wang, et al., Atomic-layer-deposited ZnO on carbon black as high-performance catalysts for the thermal decomposition of ammonium perchlorate, *Powder Technol.* 25 (2017) 3154–3160. <https://doi.org/10.1002/ejic.201700146>.
- [42] S.G. Hosseini, R. Ahmadi, A. Ghavi, et al., Synthesis and characterization of  $\alpha$ -Fe<sub>2</sub>O<sub>3</sub> mesoporous using SBA-15 silica as templater and investigation of its catalytic activity for thermal decomposition of ammonium perchlorate particles, *Powder Technol.* 278 (2015) 316–322. <https://doi.org/10.1016/j.powtec.2015.03.032>.
- [43] Y. Li, S. Zhu, X. Liu, et al., Research progress in thermal decomposition mechanism of ammonium perchlorate, *Chem. Propell. Ploym. Mater.* 1 (2015) 32–37. <https://link.oversea.cnki.net/doi/10.16572/j.issn1672-2191.2015.01.027>.
- [44] H.T. Feng, X.J. Liu, Y. Li, et al., Novel powder catalysts of ferrocene-based metal-organic framework and their catalytic performance for thermal decomposition of ammonium perchlorate, *Powder Technol.* 397 (2022) 117035. <https://doi.org/10.1016/j.powtec.2021.117035>.
- [45] S. Nair, S. Mathew, C.P. Regunadhan Nair, High energy materials as thermal decomposition modifiers of ammonium perchlorate, *Mater Today Proc.* 25 (2020) 144–147. <https://doi.org/10.1016/j.matpr.2019.12.203>.
- [46] N. Yadav, P.K. Srivastava, M. Varma, Recent advances in catalytic combustion of AP-based composite solid propellants, *Def. Technol.* 17 (2021) 1013–1031. <https://doi.org/10.1016/j.dt.2020.06.007>.
- [47] S. Lashgari, M.S. Baei, F.F. Abkanar, et al., Catalytic effect of solvothermally prepared Cu<sub>2</sub>(bdc)<sub>2</sub>(bpy) metal-organic framework on thermal decomposition of ammonium perchlorate, *J. Solid State Chem.* 295 (2021) 121940. <https://doi.org/10.1016/j.jssc.2020.121940>.
- [48] W. Zhang, X. Zhou, T. Bao, et al., *Calculation principle of solid propellant properties*, Science Press, Beijing, 2019.
- [49] Z. Guo, Q. Zhang, H. Liu, et al., A novel metal-organic framework precursor strategy to fabricate sub-micron CuO microspheres for catalytic thermal decomposition of ammonium perchlorate, *Mater. Today Commun.* 26 (2021). <https://doi.org/10.1016/j.mtcomm.2021.102139>.
- [50] M. Usman, H. Yu, L. Wang, et al., Synthesis of ferrocenylated -aminopyridines and ferrocenylated-aminothiazoles and their anti-migration and burning rate catalytic properties, *J. Organomet. Chem.* 920 (2020) 121336. <https://doi.org/10.1016/j.jorganchem.2020.121336>.
- [51] T. Chen, Y. Hu, C. Zhang, et al., Recent progress on transition metal oxides and carbon-supported transition metal oxides as catalysts for thermal decomposition of ammonium perchlorate, *Def. Technol.* 17 (2021) 1471–1485. <https://doi.org/10.1016/j.dt.2020.08.004>.